ELSEVIER

Contents lists available at ScienceDirect

Mechanics of Materials

journal homepage: www.elsevier.com/locate/mecmat



Research paper

Mechanical structure-property relations in flexible silica-aerogels

Max Zinke a,b, Barbara Milow a,c, Gunnar Seide b, Ameya Rege a,d, **

- ^a Institute for Frontier Materials on Earth and in Space, German Aerospace Center (DLR), Cologne, 51147, Germany
- ^b Aachen-Maastricht Institute for Biobased Materials (AMIBM), Maastricht University, Geleen, 6167 RD, The Netherlands
- ^c Institute of Inorganic and Materials Chemistry, University of Cologne, Cologne, 50939, Germany
- d Department of Mechanics of Solids, Surfaces & Systems, University of Twente, Enschede, 7500 AE, The Netherlands

ARTICLE INFO

Keywords: Aerogel Flexible Mechanics DIC Inelasticity Finite element method

ABSTRACT

Flexible aerogels exhibit unique mechanical properties, yet standardisation in their testing methodologies remains limited. This study investigates the tensile and compressive behaviour of flexible aerogels through experimental and computational approaches. Cyclic compression tests are performed to assess damage evolution, while digital image correlation is utilised to measure lateral strain and evaluate the influence of different spraying patterns on strain measurement accuracy. Challenges associated with tensile and compressive testing are critically analysed, highlighting inconsistencies in current practices. Finite element modelling is employed to examine the role of friction in inducing the barrelling effect under compressive loads. The findings underscore the necessity for standardised mechanical testing protocols for flexible aerogels and provide insights into their deformation behaviour under various loading conditions.

1. Introduction

Silica aerogels are a fascinating class of highly porous materials known for their unique combination of properties, including extremely low density, high surface area, and remarkable thermal insulating capabilities (Hüsing and Schubert, 1998). They are synthesised by means of the sol–gel process of gelation followed by supercritical or ambient pressure drying. The resulting nanostructured network gives them their extraordinary characteristics. As a result, they have diverse applications, from thermal insulators in spacecraft to components in energy storage and environmental remediation (Hrubesh, 1998; Smirnova and Gurikov, 2018). Their ability to withstand extreme temperatures and their low thermal conductivity make them invaluable in industries where insulating materials need to perform in demanding conditions.

However, despite their remarkable properties, silica aerogels are highly fragile, limiting their range of applications and posing challenges for use in environments where mechanical stability is essential. To this end, diverse approaches to flexiblise silica aerogels have been proposed. These include physical reinforcement or chemical modification of the silica backbone. Examples of physical reinforcement may include infiltrating the sol with a fibre batting (Parmenter and Milstein, 1998; Heyer et al., 2020; Almeida et al., 2021) or a honeycomb matrix (Schwan et al., 2015; Bhuiya et al., 2016) or a foam scaffold (Merillas et al., 2022a,b). On the other hand, the now common approach to chemically modify the aerogels for making them flexible tends towards using organoalkoxysilanes as precursors. Rao

et al. (2006) first proposed the synthesis of flexible aerogels using the methyltrimethoxysilane (MTMS) precursor. In another study, Guo et al. (2009) proposed using bis[3-(triethoxysilyl)propyl]disulphide and vinyltrimethoxysilane to flexiblize silica aerogels. These two breakthrough studies were followed by Hayase et al. (2011) who proposed using MTMS and dimethyldimethoxysilane (DMDS) to develop flexible aerogels and xerogels. These are now commonly referred to as marshmallow aerogels in the literature, due to their marshmallowlike appearance. The same research team in a later study reported on superflexible transparent aerogels from polyvinylpolymethylsiloxane (Zu et al., 2018). There have been other reports on flexiblisation of aerogels. While most of these approaches result in flexible aerogels, they often remain very soft demanding additional reinforcement to increase their stiffness (Rege et al., 2019). Increased stiffness is often demanded for practical applications, e.g., for insulating spacecrafts or satellite components. Testing for characterisation purposes is also affected by the very low stiffness of the aerogel, resulting in diverse issues, including but not limited to specimen clamping. This demands an in-depth understanding of their (in-)elastic properties.

In this paper, we report on the mechanical characterisation of flexible aerogels. A heuristic study on the tensile and compressive characteristics of these aerogels is reported. Furthermore, cyclic compression is undertaken to observe the damage evolution in the aerogels. Digital image correlation (DIC) is used to study the longitudinal and

^{*} Corresponding author at: Department of Mechanics of Solids, Surfaces & Systems, University of Twente, Enschede, 7500 AE, The Netherlands. E-mail address: ameya.rege@utwente.nl (A. Rege).

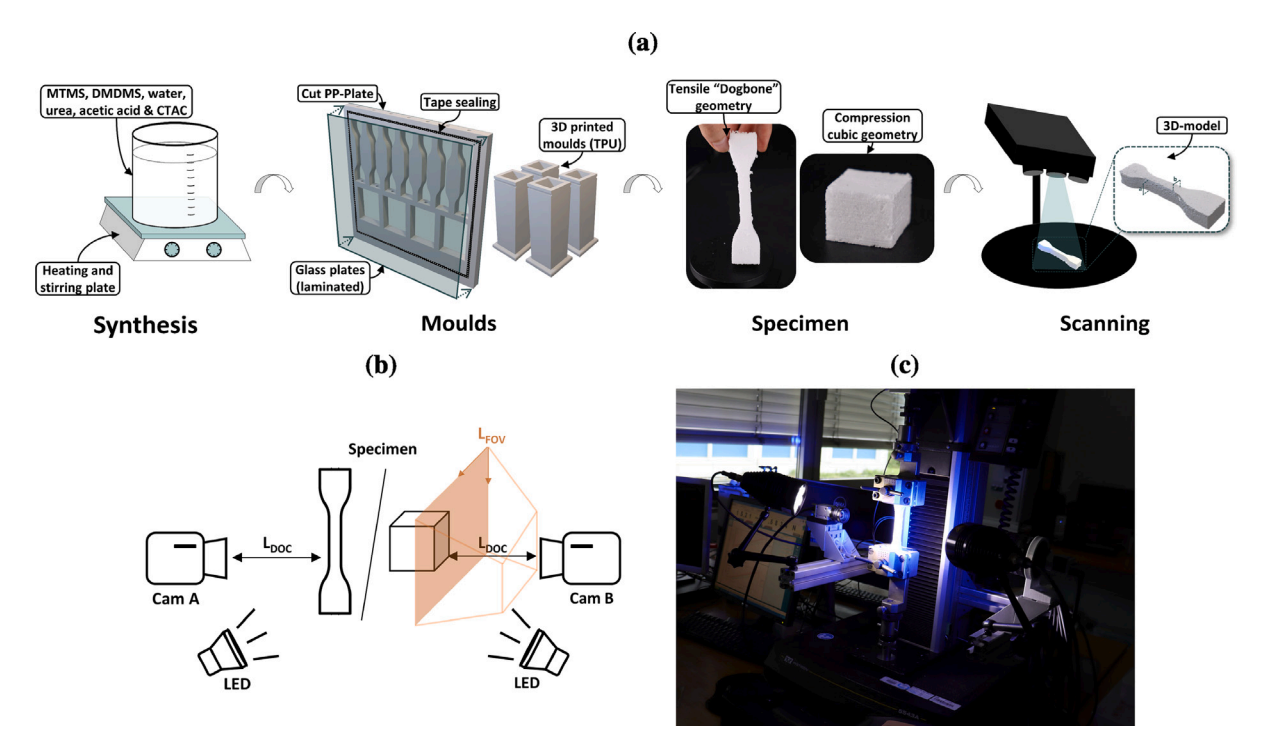


Fig. 1. Methodology showcase (a) Creation and characterisation of specimens using specific moulds and 3D-Scanning (b) Scheme of the setup used for DIC (c) Tensile testing of a dogbone geometry.

lateral strain in the aerogels. The study also aims at motivating standardisation for mechanical testing of aerogels. There is a significant gap in the uniformity of testing methods for aerogels, including those in consideration for such flexible aerogels. To this end, challenges in tensile and compression testing of such aerogels are discussed in this paper. The choice between different patterns of spraying for DIC and their resulting characteristics on aerogels are discussed in detail. Finally, the finite element modelling is applied to study the effect of friction that results in the bulging behaviour under compression.

2. Methodology

2.1. Materials

2.1.1. Preparation of moulds

In order to synthesise the flexible silica-aerogels, the first step was to create moulds that matched the final specimen geometries required for the mechanical tests. This was done to minimise the necessity for post-processing of the specimens after drying, which could otherwise result in pre-stress or even damage occurring during the cutting of the specimens. A particular challenge arises during gelation, where unreacted sol residues build up on top of the gel, resulting in an uneven surface on the top of the gel body. Therefore, the moulds were positioned vertically during gelation, ensuring that only the sides of the specimens oriented upwards that were irrelevant for the tests (e.g. the respective longitudinal ends of bar specimens).

For the tensile specimens, dogbone-shaped geometries following the type 1 A according to DIN EN ISO 1798 were cut from a 15 mm thick PP plate. Additionally, cuboid bar geometries having a width of 35 mm and a length of 150 mm were prepared for comparison. Furthermore, holes with a diameter of 6 mm were drilled on the top side to enable the filling of the mould. Then, the cut PP-Plate was clamped laterally on both sides with 250 \times 250 mm glass plates. Prior to this, the glass plates were laminated with a polyester based film using an iron at 130 °C. A flexible tape made of EPDM rubber was used as a sealing material between the plate and the glass.

To test the compression characteristics, cuboid moulded specimens measuring 20 mm on each side were produced instead of cylindrical specimens, due to their smaller barrelling. The equivalent moulds having dimensions of $70 \times 20 \times 20$ mm were made using the *Snapmaker Artisan* 3D printer. TPU filament was used due to its good resistance to the sol and gelling temperature. Both moulds are shown in Fig. 1a.

The specimen geometries were captured using the 3D Scanner GOM Atos ${\bf Q}$ with MV270 lenses.

2.1.2. Synthesis of aerogels

The synthesis of the flexible silica aerogels was carried out using a combination of trifunctional methyltrimethoxysilane (MTMS) and difunctional dimethoxydimethylsilane (DMDMS) precursors, following the method optimised by Fener and Niemeyer (2016). Firstly, urea and glacial acetic acid were dissolved in deionised water at 50 °C with continuous stirring 200-300 rpm using a cross-shaped magnetic rod. Subsequently, a hexadecyltrimethylammonium chloride solution (25 wt. % in water, CTAC) and MTMS were added, with CTAC functioning as a surfactant. Both were homogenised at 50 °C for 15 min. In a final step, DMDMS was added to the mixture and homogenised at 50 °C for a further 45 min. The molar ratios of the components were approx. 1 (MTMS): 0.69 (DMDS): 40.67 (water): 4.06 (urea): 3.56×10^{-3} (acetic acid): 0.12 (CTAC). The specimens were gelled and aged in an oven at 80 °C for 24 h. Finally, the specimens were subjected to a three-stage washing process, wherein they were immersed in water, ethanol, and deionised water, respectively, for a duration of two cycles. Each cycle lasted at least 8 h and the volume of solvent employed for each wash was approximately twice that of the specimens.

Finally, the specimens were dried at 80 $^{\circ}$ C for at least 15 h. While the tensile specimens were directly gelled into the desired shape, the specimens made using 3D printed moulds were carefully cut to a length of 20 mm after drying using a razor blade to obtain near perfect cubic specimens needed for compression testing.

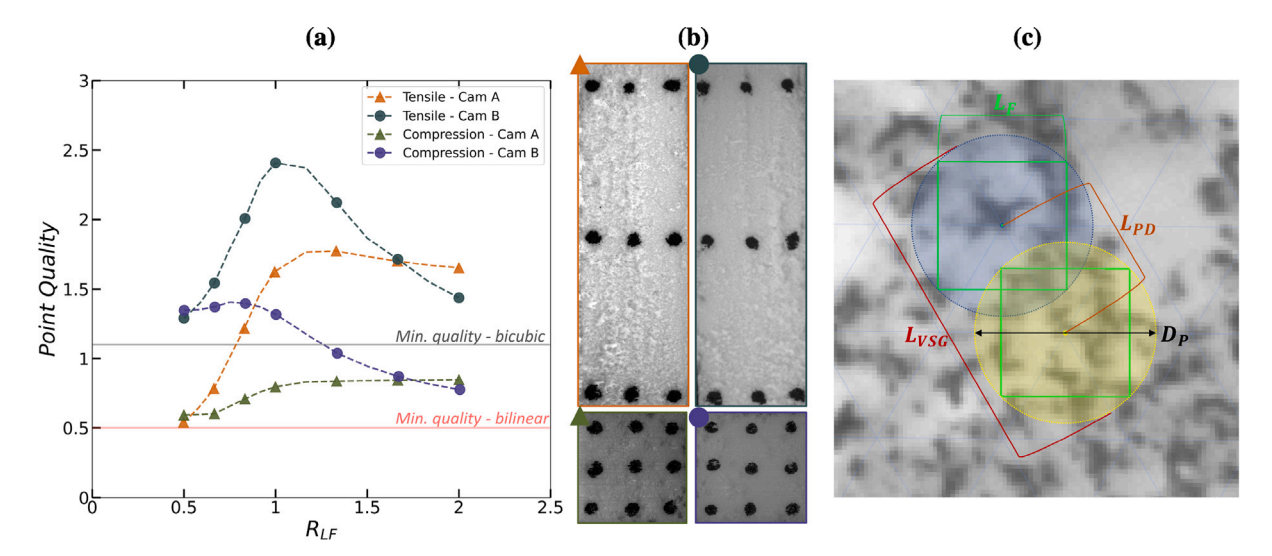


Fig. 2. Consideration of DIC software parameters (a) Mean point (QOI) quality of tensile and compression specimens as a function of the facet ratio R_{LF} (b) Respective images of the in (a) analysed tensile and compression specimens marked by the 9-Dot method (c) Scheme of DIC correlation parameters influencing the mesh fineness including the facet size L_F , the point distance L_{PD} , the point diameter D_P and the length of the virtual strain gauge L_{VSG} .

2.2. Methods

2.2.1. Tensile and compression testing

The tensile and compression tests were carried out on a universal testing machine (*Instron model 5543A*) (see Fig. 1c). A load cell with a maximum load of 50 N was used. For the tensile tests, a fixture with a corrugated surface was used. The tests were conducted with a quasistatic setup at a strain-rate of 1 mm/min. All tests were carried out until specimen failure.

In contrast, cylindrical plates were used for the compression testing. In order to obtain a representative modulus of elasticity and to investigate the flexibility of the material, cyclic tests were chosen and carried out at a strain-rate of 1 mm/min, with the maximum compressive strain increasing with each cycle (20%–40%–70%–80%). The elastic modulus was calculated from the slope of the initial linear part of the measurement.

2.2.2. DIC setup and sensitivity

In addition to the longitudinal strain captured by the traverse path, lateral strain was recorded using DIC. Two cameras with one flashlight on each side were used as a 2D system, recording each a opposite side of the specimens during the tests (see Fig. 1b). This is based on the DIC setup used for polymer foams by Marter et al. (2018). The utilisation of two cameras enables the identification of potential deviations on one side of the surface, for instance, as a consequence of an unequal clamping of the sample and an associated uneven distribution of elongation or compression. In such instances, the system is capable of compensating for these deviations by utilising average values. Additionally, the DIC system is able to record the final tear, which can occur on any side of the specimen, during tensile tests.

Two DIC patterns were tested: On the one hand, a classical speckle pattern of random distribution was applied to the tensile and compression specimens by overspray method with a spray can, resulting in a speckle size of approximately $100{\text -}600~\mu\text{m}$. Such a technique has been applied previously to study the mechanics of silica as well as carbon aerogels (Haj-Ali et al., 2016; Rege et al., 2020). On the other hand, a simplified pattern consisting of 9 dots at a pre-defined distance (Marter et al., 2018) was adjusted and applied on the aerogels, which can significantly reduce the software calculation and evaluation time. To test this 9-Dot method, a three-by-three pattern of dots having a diameter about $1.5{\text -}2.0~\text{mm}$, depending on the local surface condition, was applied to the dogbone-shaped specimens starting from the centre

of the specimen using a felt-tip pen. The horizontal spacing of the dots was approximately 5 mm and the vertical spacing approximately 18 mm. Similarly, the dots were applied to the cubic compression test specimens at a horizontal and vertical spacing of approximately 6 mm and a dot diameter of approximately 2.5–3.0 mm.

Further details of the DIC hardware can be found in the supplementary information.

In this work, the GOM Correlate software was used to analyse the data. Depending on the pattern method, the software generates single or multiple facet points, which are referred to as quantities of interest (QOIs). These are combined and tracked, enabling the calculation of strain. Each QOI defined by the software is identified via a stochastic pattern structure. For this, a correlation parameter, the facet size L_F, which defines the local area of the QOI observed for the strain calculation, was specified to the software. In order to achieve optimal recognition of a facet, it is essential that the grey value distribution is as distinct as possible. In this context, GOM defines an equivalent 'point quality' for single QOIs. This has an impact on the interpolation method employed by GOM to calculate the strain distribution for QOIs integrated into surface components. For a bicubic interpolation (higher accuracy), a point quality of at least 1.1 must be present. Conversely, a bilinear interpolation (lower accuracy) can be applied when a point quality of at least 0.5 is present.

In order to analyse the aerogel specimens marked with the 9-Dot method, nine QOIs were created and tracked on each side of the specimen. To define a suitable facet size L_F for the strain calculation of the GOM software, individual images of specimens at zero load were loaded into the software and QOIs with different facet sizes were generated while observing the QOI quality. Fig. 2a shows the mean QOI qualities of representative specimens, each comprising 9 QOIs on one side, as a function of the ratio R_{LF} defined as the selected software facet size L_F in relation to the actual mean dot size marked on the aerogel surfaces. It is evident that the curves typically pass through a maximum point quality near a ratio of 1, which corresponds to a facet size L_F that is equal to the average actual dot size. Furthermore, an increase of LF beyond the actual size of the marked dot does not necessarily result in an increase in quality, since there is no additional gain in contrast. In the case of the camera B recordings, it even leads to a lower quality. This discrepancy is likely due to the inferior quality of the image recordings of camera B, as discussed in the supplementary information. Interestingly enough, this results in a superior maximum point quality of the camera B images, provided that the chosen facet size LF lays within the actual

Experimental

Simulation [Abaqus]

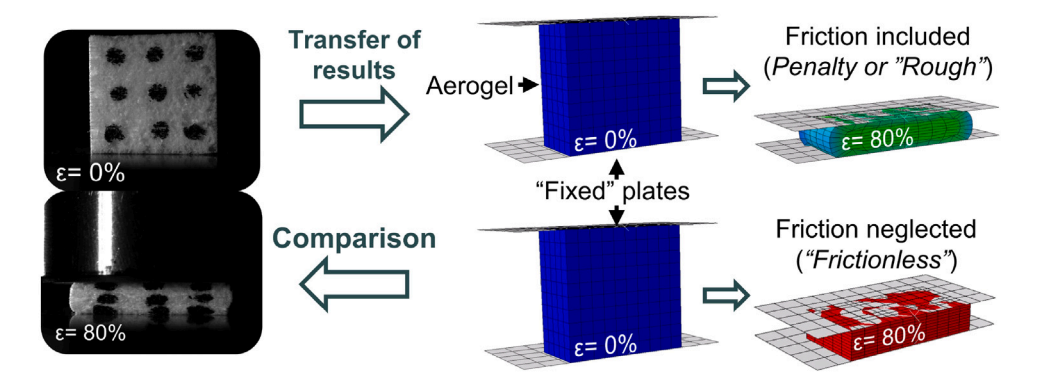


Fig. 3. Abaqus simulation scheme.

marked dot. This could be due to the higher variation in black tones (the higher grey values) compared to camera A. However, as soon as the size of the actual point is exceeded, the measurement noise of the lower contrast becomes evident, particularly due to the bright tones of the unmarked aerogel. This causes a significant decline in the point quality.

In accordance with these findings, the facet size L_F was consistently set to reflect the mean actual point size of the markings. Thus, a higher quality bicubic interpolation would be possible for most points, with the exception of the camera A recordings of the compression tests.

In the case of the overspray method, multiple QOIs were generated over a specific area, the so-called region of interest (ROI), and grouped into an surface component. Consequently, instead of examining individual points, an average strain is calculated by correlating several QOIs. This approach has the advantage of reducing the impact of noise errors of individual QOIs, by considering an average strain. Also, the failure behaviour can be examined more precisely over the ROI, e.g., using colour grading.

Compared to the 9-Dot method, in addition to defining a facet size $L_{\rm F},$ a point distance $L_{\rm PD}$ was defined as a correlation parameter. This corresponds to the distance between the centre of two neighbouring QOIs. A reduction of $L_{\rm PD}$ will result in a greater number of QOIs being generated within the ROI, therefore increasing the QOI density. Consequently, $L_{\rm F}$ and $L_{\rm PD}$ influence the fineness of the mesh.

A typical quantity derived in this context is the so-called virtual strain gauge (VSG). According to the good practices guide of the international digital image correlation society (iDICs), a VSG describes the size of the local area within the region of interest (ROI) that influences the strain value at a specific location, comparable to a physical strain gauge (Jones and Iadicola, 2018). The relationship between the correlation parameters of the GOM Software, the facet size L_F and the point distance L_{PD} , and the resulting VSG can be illustrated according to Fig. 2c: Two neighbouring QOIs with the facet size L_F have a defined point distance L_{PD} (centre to centre). Additionally, a point diameter D_P is defined, which represents the size of the area around the centre of a QOI that is used to calculate the strain. This corresponds to the diagonal of the facet point multiplied by a so-called strain neighbourhood tensor δ_{St} .

$$D_{\rm P} = \delta_{\rm St} \cdot \sqrt{L_{\rm F}^2 + L_{\rm F}^2}$$

$$= \delta_{\rm St} \cdot \sqrt{2} \cdot L_{\rm F}$$
(1)

With consideration of Eq. (1), the length of the VSG L_{VSG} can be described as

$$L_{\text{VSG}} = L_{\text{PD}} + D_{\text{P}}$$

= $L_{\text{PD}} + \delta_{\text{St}} \cdot \sqrt{2} \cdot L_{\text{F}}$ (2)

An increase of L_{VSG} , the area around a calculation point considered, will result in a reduction in noise and an improvement in accuracy, as local fluctuations in strain will be smoothed out. Conversely, however, fine features and deformations cannot be distinguished from noise with a higher L_{VSG} , resulting in a worse spatial resolution (Jones and Iadicola, 2018; Merzkirch, 2022).

In the case of flexible silica aerogels, the ability to detect and follow larger tears and localised deformations that may occur is of particular importance, given the anticipated large deformations. It is essential to ensure that the detection and monitoring of these deformations is accurate, while maintaining precision at smaller scales. The $\rm L_{VSG}$ for the DIC setup used in this work was therefore selected individually for both tensile and compression tests, with the objective of minimising measurement noise without the significant reduction of the measurement resolution. For further details regarding the selected DIC software parameters, please refer to the supplementary information.

2.3. Finite element modelling

To analyse the influence of friction between the specimen and the compression plates on the resulting compressive behaviour, finite element analysis (FEA) was conducted. The FEA was carried out using Abaqus. Given the expected high deformation of the flexible silica aerogels and their inherent flexibility, a hyperelastic material model tailored for porous materials was chosen. To this end, the so-called 'Hyperfoam' model, based on the Ogden–Hill model for large deformations of incompressible solids (Ogden and Hill, 1972; Hill, 1979), which was adapted and simplified by Storåkers (1986), among others, was employed. The strain–energy function is described as

$$W = \sum_{i=1}^{N} \frac{2\mu_i}{a_i^2} \left[\lambda_1^{\alpha_i} + \lambda_2^{\alpha_i} + \lambda_3^{\alpha_i} - 3 + \frac{1}{\beta_i} \left(J^{-\alpha_i \beta_i} \right) \right], \tag{3}$$

where the parameter N represents the order of the function, while the parameters μ_i , α_i and β_i are temperature-dependent material parameters. Furthermore, the principle stretches λ_i and the total volume ratio J (current volume divided by the original volume) are considered. Experimental stress–strain curves, including lateral strain, from different types of tests can be used as input. In the case of uniaxial test data, the nominal stress (first Piola–Kirchhoff Stress P) is calculated according to

$$\mathbf{P} = \frac{\partial W}{\partial \lambda_C} = \frac{2}{\lambda_C} \sum_{i=1}^{N} \frac{\mu_i}{\alpha_i} \left[\lambda_C^{\alpha_i} - J^{-\alpha_i \beta_i} \right]$$
 (4)

for each experimental stress–strain pair, with λ_C being the stretch in the primary displacement direction. Furthermore, a measurement error is defined for each n_{th} data pair according to

$$E = \sum_{i=1}^{n} \left(1 - \frac{P_i^{sim}}{P_i^{exp}} \right)^2 \tag{5}$$

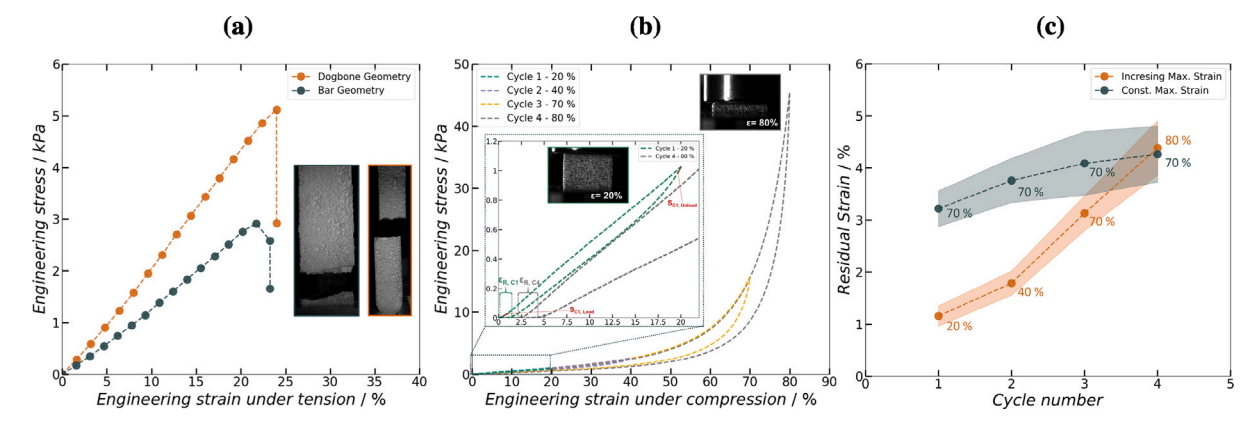


Fig. 4. Mechanical testing results (a) Stress-strain curves of flexible silica aerogel bar and dogbone specimens subjected to tensile load, along with the statistical parameters and representation of the characteristic tearing behaviour (b) Stress-strain curves of cubic flexible silica aerogel specimens subjected to cyclic compression tests (varying residual strains visible at 1–20 strain-% magnification) (c) Comparison of residual strain as a function of the maximum compressive strain and the number of cycles.

This error corresponds to the simulated and experimental nominal stress, denoted by P_i^{sim} and P_i^{exp} , respectively. The experimental stress-strain data from uniaxial tests, as well as the lateral strain data derived from DIC results, are given as an input to the Hyperfoam model in Abaqus in a tabular format in steps of 10% strain. This results in a total of 10 data points. The lateral strain data is used by the model to compute the transverse stretches λ_2 and λ_3 . Once the experimental data has been input, the material parameters for which the measurement factor E is minimised are derived using the non-linear least squares method.

In the case of the investigation of the flexible silica aerogel, a model is first created that mimics the behaviour observed in the experiment: An experimentally determined representative stress–strain curve of the compression tests (first cycle) and the corresponding lateral strain recorded using DIC served as input. These are used according to Eq. (3) to derive a second-order strain–energy function for which the best agreement can be found. For this purpose, a cubic solid element model, with dimensions similar to those in the experiment (20 mm each side) was created, which represents the flexible silica aerogel. In contrast, two rigid shell elements (35 \times 35 mm) were created as planar pressure plates and placed on the top and bottom of the cube (see Fig. 3). While the lower plate was "encastred", the upper plate is given one degree of freedom in the primary direction of displacement. During the simulation, the upper plate is compressed by 80%.

The type of interactions between the aerogel and the pressure plate elements were defined as *surface* to *surface* contacts and varied, ranging from *Rough* (friction coefficient =1) to *Frictionless* (friction coefficient =0). On the one hand, a square, planar mesh (*R3D4*) was selected for the rigid pressure plates, while on the other hand, 8-sided, linear bricks (*C3D8R*) were generated for the aerogel cube.

3. Results and discussion

3.1. Tensile tests: Comparison of dogbone-shaped and bar specimens

The results of the tensile test, in which two test geometries were compared, are presented in Fig. 4a. The stress–strain curves demonstrate that the aerogels are capable of undergoing deformation over 20% strain, beyond which they exhibit failure. The deformation was observed to be nearly linear. The elastic modulus and the tensile strength were determined and are presented in Table 1. The tensile strength is defined as the maximum stress, while the elastic modulus as measured under tension was determined within the range of 0.25 to 0.50% elongation.

It is observed that the simple bar geometry exhibits a markedly flatter curve with a lower maximal stress in comparison to the dogboneshaped specimen. Consequently, for the dogbone-shaped geometries

Table 1
Tensile testing — material properties.

| | Bar Geometry | Dogbone-shaped Geometry |
|-----------------------|------------------|----------------------------|
| Tensile strength/kPa | 2.9+0.2 | 5.2+0.2 |
| Elastic Modulus/kPa | $10.5_{\pm 0.4}$ | 18.3 _{±2.7} |
| Elongation at break/% | $24.3_{\pm 2.0}$ | $23.9_{\pm 3.9}$ |

the mean tensile strength was 5.2 kPa and the elastic modulus was 18.3 kPa, nearly 70% higher than the values obtained for the tested bar geometries. This difference could be linked to the resulting inhomogeneous stress distribution in the simple bar geometry case. While the dogbone-shaped specimens failed within the constricted cross-section area, the bar specimens failed near or within the clamping area. This leads to an overestimation of the actual cross-section undergoing deformation and therefore, an underestimation of the stress. Therefore, a dog-bone shape is preferred for tensile test specimens because it concentrates stress in the middle, ensuring failure occurs in the intended gauge section, rather than at the clamps. Interestingly, a comparable maximal strain was observed, indicating that other effects besides the geometry also have an influence on the maximal strain. It is assumed that this phenomenon is caused by the formation of macropores (≥ 1 mm) in the outer region of the specimens. This formation can be observed as a result of the gas phases that are generated during the synthesis process, which remain attached to the mould and to the already gelled agglomerates. In the case of uniaxial testing, the force is distributed over the cross-section. The formation of macropores may result in the initiation of tears at a faster rate due to the presence of stress concentrations.

Consequently, optimising the synthesis process may be a viable approach, whereby the gelation process could be accompanied by an ultrasonic bath or a similar method to prevent the formation of macropores. This could lead to more conclusive results regarding the final strain. Nevertheless, the data suggests that a maximum tensile strain above 20% elongation was reached.

3.2. Compression tests: Inelasticity under step-wise increasing cyclic deformation

The outcomes of the cyclic compression tests are illustrated in Fig. 4b. The results presented here are those observed for a representative specimen. The stress–strain curve is colour-coded according to the independent cycles. The deformation exhibits characteristics indicative of highly flexible cellular material behaviour. It does not display a well-defined plateau region. Instead, it demonstrates buckling of pore walls, followed by pore collapse and subsequent densification.

 Table 2

 Cyclic compression testing — material properties.

| | Values | | | | |
|---|----------------------------|---|-------------------------------------|--|--|
| | $\epsilon = 0\%$ (loading) | $\epsilon = 20\%$ (unloading) | $\epsilon = 40\%$ (unloading) | $\epsilon = 70\%$ (unloading) | $\epsilon = 80\%$ (unloading) |
| Compressive Strength \ kPa Elastic Modulus \ kPa | - 5.9 _{±0.6} | 1.1 _{±0.1} 11.5 _{±1.0} | $2.6_{\pm 0.2}$ $33.1_{\pm 3.0}$ | 15.6 _{±1.2} 416.5 _{±42.9} | 43.4 _{±4.6} 1661.6 _{±236.7} |

It can be observed that silica aerogels do not exhibit linear elastic behaviour even at small strains due to inelastic deformations. This was also shown in previous studies (Patil et al., 2017; Fekadu et al., 2022). Given this high nonlinear behaviour of the aerogels, the elastic modulus is determined from the unloading curve, on the assumption that the material can be considered to react fully elastically. This can be explained as follows: The elastic modulus is typically measured from the linear regime of the loading part of the stress-strain curve. This region exhibits purely elastic regime, as is in generally the case with metals. However, for materials like the flexible aerogels, this region is not explicitly linear, due to inelastic deformation. To obtain the elastic modulus, one must closely look at the definition of elasticity. It is the stress driven deformation related to the energy that can be fully recovered as efficient mechanical work. In fact, it is the unloading phase of the quasi-static test where the mechanical work is provided by the material. Thus, the slope of the unloading curve gives a reliable estimation of the elastic modulus. For better understanding, the slopes of the loading (S_{Load}) and unloading curve (S_{Unload}) of the first cycle are shown in Fig. 4a.

The mechanical properties in relation to the maximal compressive strain are presented in Table 2. It shows the increase in elastic modulus with increasing strain. This can be attributed to a decrease of porosity, like it is typically done for porous materials.

Furthermore, an examination of the hysteresis of the unloading curves is also of interest: While in the initial cycle, a minor hysteresis is evident, indicating pronounced elastic deformation, increasing inelastic deformation of the material can be observed at higher maximal compressive strains in subsequent cycles. This phenomenon could be attributed to the reduction in material resistance exhibited by the specimen during the unloading process, due to a gradual recovery of deformed pores. This is also evident in the expanded partial representation of the diagram in Fig. 4b. It is evident that the loading curves of the various cycles are becoming increasingly divergent, as shown for cycles 1 and 4.

From a mathematical perspective, the strain at the point of the initial increase in force or stress of the loading curve ($\epsilon_{0\text{-loading}}$ at the point of the first guaranteed specimen contact) can be compared with the strain at the point of the first zero load during unloading ($\epsilon_{0\text{-unloading}}$ at guaranteed loss of contact with the specimen) in order to calculate a residual strain ϵ_{R} in accordance with the Eq. (6).

$$\epsilon_{\rm R} = \epsilon_{\rm 0-deloading} - \epsilon_{\rm 0-loading}$$
 (6)

The correspondingly calculated residual strain is illustrated in Fig. 4c as a function of the cycle number and the maximal compressive strain. The initial curve illustrates a rising residual strain for an increased maximal compressive strain with each cycle, from approx. 1 to 4.5%, which clearly demonstrates the increasing inelastic deformation. Furthermore, this method can be employed to gain additional details regarding the nature of the inelasticity. To illustrate, the second curve depicts a distinct cyclic mode in which the material was compressed over four times with up to 70% of compressive strain within each cycle. It can be observed that directly loading and unloading up to 70% compressive strain reduces the same amount of residual strain as loading and unloading step-wise from 20 to 40 and 70%. Moreover, undertaking cyclic deformation multiple times at the same maximal strain results in an increase in the amount of residual strain. In the final cycle, the residual strain after 70% compression is found to be almost identical to

Table 3Comparison of overspray and 9-Dot DIC results for step-wise analysis under tension.

| | Traverse Path | Overspray Method | 9-Dot Method |
|----------------------------------|----------------------|----------------------|----------------------|
| Elastic Modulus/kPa | 18.3 _{±2.7} | 19.2 _{±4.6} | 16.3 _{±4.3} |
| Elongation at break/% | $23.9_{\pm 3.9}$ | $22.2_{\pm 4.4}$ | $24.4_{\pm 4.2}$ |
| Difference to reference/strain-% | - | $0.5_{\pm 0.1}$ | $1.1_{\pm0.6}$ |

that of the first curve at 80% compressive strain, with a residual strain of approximately 4%.

The results demonstrate that the marginal residual strain, which indicates the material's pronounced flexibility and elasticity, also exhibits a dependency on the number of cycles. It can be hypothesised that this phenomenon can be attributed to the deformation of specific pores being "shielded" through the deformation of other pores, until they are also compressed through repeated loading. It should also be noted that this form of observation reflects the direct residual strain occurring immediately after the unloading of the specimens, as a function of the relaxation time limited by the test speed. Whether the material achieves complete recovery has not been investigated.

3.3. Inference from digital image correlation

The objective of the DIC tests is twofold: primarily, the tests provide a more detailed analysis with regard to the formation of tears and the distribution of stress. Secondly, the tests aim to record the lateral strain necessary for the FEA. As previously stated, two additional analysis methods, namely the overspray and the 9-Dot method, were employed, and sensitivity analyses were conducted for each of these, to assure high quality output while using a widely available and reproducible two-camera system.

Furthermore, two calculation methods were undertaken and are presented for the resulting DIC stress–strain curves. The two analyses are the so-called *reference analysis* and the *step-wise analysis*. In the reference analysis, the strain calculation for each image, is related to an original reference image. In this case, the reference image represents a zero load state. This approach allows for a high level of accuracy to be achieved. However, convergence issues and longer calculation times may arise due to the increased deformation with increasing strain and the correspondingly more complex identification of the QOIs. An alternative is the step-wise analysis, in which the strain calculation of each image is related to the previous one. This enables better convergence with shorter calculation times, even with large deformations. However, measurement errors get compounded per image instance.

The two analysis methods are compared in Fig. 5a and b, which show images of two representative dogbone specimens: one prepared by the overspray method and the other by the 9-Dot method. The images are presented as seen shortly before the specimens failed. In the case of the overspray method, it becomes evident how a colour-grading of the region of interest (ROI) is created based on the strain results of the OOIs.

For the displayed specimen, it is observed that there are gaps in the ROI within the area of larger strains or tears, as observed in the reference analysis.

This is a consequence of the exclusion of QOIs due to an inadequate degree of conversion with the reference image. In contrast, the

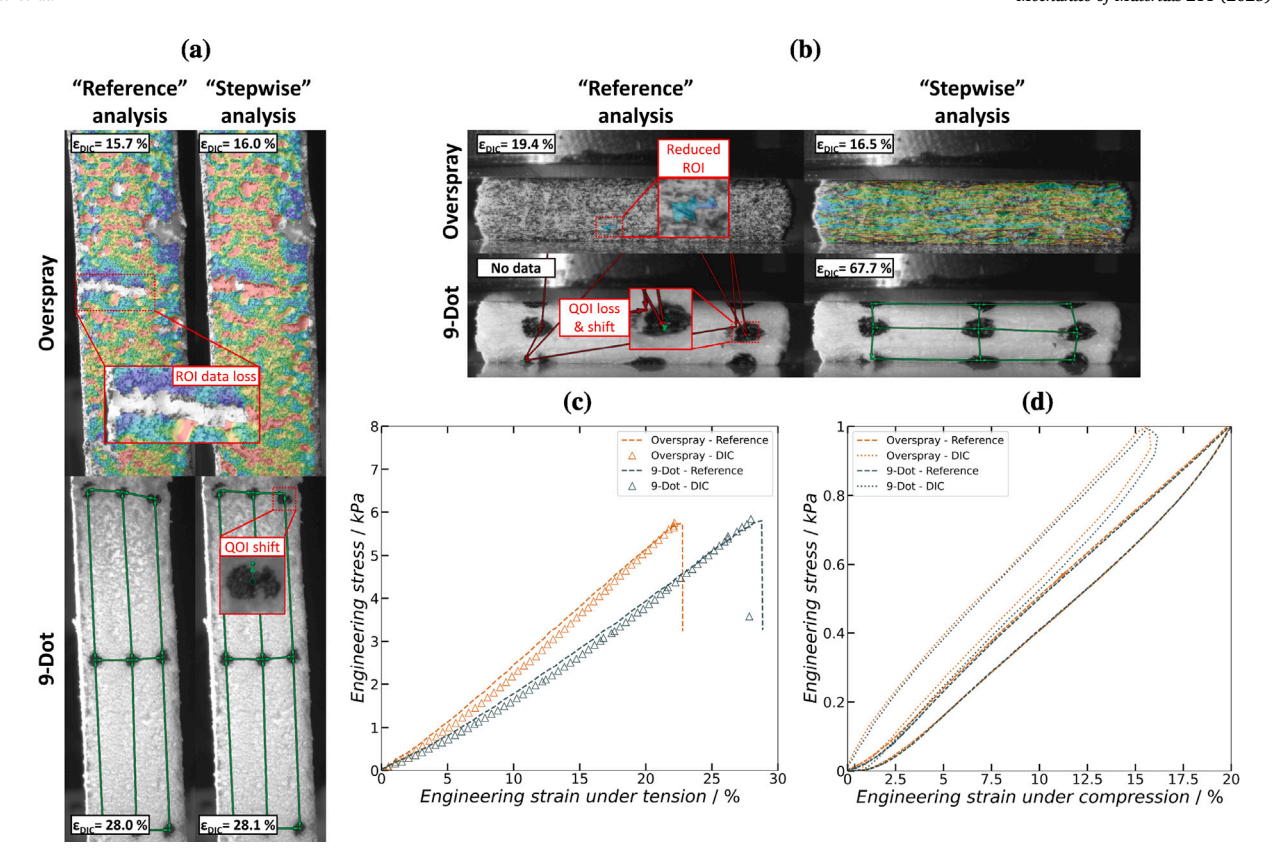


Fig. 5. Results of digital image correlation (DIC) (a) Strain distribution of the *reference analysis* and *step-wise analysis* for an overspray and a 9-Dot specimen moments before failure (~24%) (b) Strain distribution of the *reference analysis* and *step-wise analysis* for an overspray and a 9-Dot specimen at 20% (left) and 80% (right) compressive strain (c) Comparison of DIC and loading machine ("Reference") stress–strain curves including mechanical characteristics of overspray and 9-Dot DIC method for tensile testing using step-wise analysis (d) Comparison of DIC and loading machine ("Reference") stress–strain curves including overspray and 9-Dot DIC method for cyclic compression testing till 20% compressive strain (Cycle 1) using step-wise analysis.

step-wise analysis allows for the observation of a significantly greater number of QOIs, even at high strains. However, in the case of the displayed specimen, the strain calculated using the step-wise analysis is found to be marginally higher than that calculated using the reference analysis. An explanation for this discrepancy could be the combination of missing QOIs representing greater strains within the ROI of the reference analysis and/or the accumulation of measurement errors within the step-wise analysis. However, the latter can be considered less significant, as the potential for measurement error (both bias and noise) was analysed and reduced through the implementation of sensitivity studies conducted previously. Furthermore, the standard strain value obtained by the traverse for the aforementioned specimen is 16.7%, thereby demonstrating that the result of the step-wise analysis is more closely aligned.

In contrast, regarding the 9-Dot method, another observation can be made. In this case, all nine QOIs converge even at large strains in the reference analysis, presumably due to their high contrast, which could explain the similar result of approximately 28% for both analysis. However, it is noteworthy that the step-wise analysis reveals a phenomenon whereby the corresponding QOI exhibits a drift due to the tearing of a marked point, as displayed in Fig. 5a. Nevertheless, it is evident that the influence on the mean strain is insignificant due to the remaining QOIs.

Thus, it can be concluded that the calculated strains are comparable. For further discussion of the tensile results, the step-wise analysis is employed, as this facilitates superior convergence for high strains, particularly with the overspray method, where more comprehensive ROIs are achieved in combination with reduced complexity and calculation time.

In Fig. 5c, the two DIC methods are compared with their respective traverse reference curves, using representative stress-train curves derived from an step-wise analysis of an overspray and a 9-Dot specimen. Furthermore, the corresponding averaged mechanical characteristic values are presented in Table 3. The DIC strain results for both the overspray and 9-Dot method demonstrate a high degree of correlation with the reference curves.

With regard to both cases, the average values are slightly lower than those of the reference, and a number of potential causes can be postulated: in addition to potential measurement uncertainties of the DIC system, which can accumulate particularly in step-wise analysis, as already described, the strains detected on the surface, for instance due to a certain strain distribution along the length of the specimen or also strain differences between the inner and outer regions of the specimen, may differ from the strain recorded by the traverse path. Nevertheless, the observable divergence of the curve does not indicate substantial influences.

The cyclic compression tests were also subjected to analysis in terms of the DIC results. Fig. 5b illustrates the calculated strains of a representative overspray and 9-Dot specimen, derived through reference analysis and step-wise analysis. In all instances, the 80% compression condition is illustrated (accordance with the traverse path). It can be observed, that the majority of the ROI within the reference analysis of the overspray specimen is lost up to 80% compression. In contrast, a substantial portion of the ROI can be preserved within the step-wise analysis even under high compression, making it crucial to ascertain the strain distribution. However, the calculated compression for the specimen shown here is only approximately 16%–20%, which is significantly below that of the traverse path.

The disparity in the quality of the two analysis methods for compression is even more pronounced for the 9-Dot method: in the case

Table 4Accuracy of the overspray and 9-Dot DIC method in the form of the respective deviation from the reference in compressive strain-%.

| | Difference from reference \ Strain-% | | |
|-------------------------------------|--------------------------------------|--------------------------|--|
| | Overspray method $(n = 4)$ | 9-Dot method ($n = 4$) | |
| Cycle 1 ($\epsilon_{Max} = 20\%$) | 3.2 _{±1.0} | 2.4 _{±0.6} | |
| Cycle 2 ($\epsilon_{Max} = 40\%$) | 8.5 _{±6.9} | $3.3_{\pm 0.6}$ | |
| Cycle 3 ($\epsilon_{Max} = 70\%$) | $17.3_{\pm 13.0}$ | $4.8_{\pm 0.6}$ | |
| Cycle 4 ($\epsilon_{Max} = 80\%$) | 22.9 _{±14.6} | $5.6_{\pm0.3}$ | |

of the reference analysis, nearly all QOIs are excluded due to a lack of convergence, resulting in an inability to ascertain the compression value. In contrast, the step-wise analysis provides access to all measured values, although it also exhibits a notable discrepancy in strain estimation, with an underestimation of approximately 12%. The challenges in conducting DIC analysis during compression arises from the extreme deformation in the direction of the camera viewing angle, which results in surfaces being partially obscured by strong barrelling. Additionally, as previously demonstrated, the lower image quality observed may be attributed to poorer exposure conditions.

Consequently, it can be stated that the step-wise analysis is a crucial component of both DIC methods in the context of compression. Therefore, it is used for the further discussion of the compression tests.

The resulting stress–strain curves of the step-wise analysis of representative overspray and a 9-Dot specimens are illustrated in Fig. 5d and compared with their respective reference curve.

Similar to the preceding calculation analysis under tension, the DIC compressive strain results exhibit notable discrepancies when compared to the reference curves. While the discrepancies remain relatively minor for the initial cycle up to 20% compressive strain, as illustrated in Fig. 5d, a notable divergence is evident with increasing compression, particularly for the overspray method. This phenomenon was observed for all specimens that underwent analysis, as illustrated in Table 4.

The table lists the mean discrepancies between the strain values obtained from DIC and those recorded mechanically via traverse path for both methods.

The deviation increases with the increasing strain for both DIC methods. At a compressive strain of 80%, the overspray method in particular exhibits a critical deviation of approximately 23% on average, with a notable fluctuation in values for different specimens. In the most extreme case, the strain observed for the overspray DIC results is lower for the final cycle than for the preceding one.

In contrast, the 9-Dot method exhibits a significantly lower average deviation of approximately 6%, with a notably reduced degree of variability for different specimens. This discrepancy in accuracy can most likely be attributed to the exclusion of QOIs in the overspray method, which encompasses only specific, statistically less deformed surface areas, resulting in a pronounced underestimation of the calculated strains. These underestimations can, in turn, result in the accumulation of errors over the course of the measurement due to the step-wise analysis. In contrast, the 9-Dot method allows for the conversion of all QOIs, whose distribution over the ROI was defined in advance, throughout all cycles. In this case, it is more probable that an underestimation of the actual strain is the result of potential drift effects observed in this regard.

In conclusion, it can be stated that both DIC methods are mostly unsuitable for the assumption of uniaxial compression in the direction of loading for large deformations. For less finite deformation, for example up to 40%, however, the recorded values using the 9-Dot method were found to be more accurate. The overspray method is less appropriate in this context, although it can yield valuable insights into the strain distribution, e.g., through colour-grading, at lower compression levels.

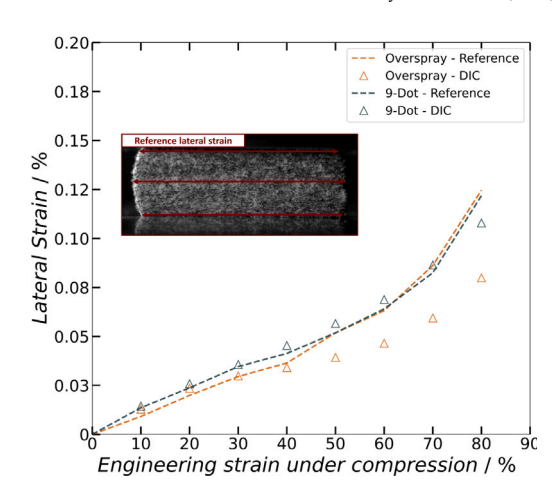


Fig. 6. Comparison of lateral strain as a function of compressive strain manually captured (reference curves) vs. automatically captured with the DIC overspray and 9-Dot method.

3.4. Effect of friction on the mechanical behaviour

In order to analyse the influence of friction between the flexible silica aerogel and the compression plates, FEA was carried out using Abaqus in accordance with the method previously described. In order to conduct this investigation, it was necessary to obtain a lateral strain as an input, which could be derived from the DIC measurements. As previously demonstrated, the DIC measurements of compressive strain in the longitudinal load direction are only reproducible under specific conditions. These conditions include moderate compression and the 9-point method with step-wise analysis. Nevertheless, it remains unclear whether DIC can also be used to record a realistic lateral strain under the same conditions.

In order to investigate this, the DIC results are initially compared with a "manual" evaluation of the lateral deformation of the compression specimens. For this, the GOM Correlate software was employed to ascertain the length per pixel in a reference image at zero load, and to monitor the external strain over three height points as a function of compressive strain. The respective results for two representative specimens of the overspray and 9-Dot method are presented in Fig. 6. The lateral strain curves exhibit a comparable characteristic progression to the stress–strain curve in the direction of loading, displaying an increase with increasing compressive strains. This phenomenon can be attributed to barrelling of the specimen.

A comparison of the DIC values for the overspray and 9-Dot method at low compressions with the respective reference curve reveals a high degree of agreement. However, similar to the observations in the case of longitudinal strain, a significantly greater deviation from the reference can be seen for compressive strains beyond 30%-40% for the overspray method. It is noteworthy that a considerably lower difference from the reference can be discerned when utilising the 9-Dot method. One explanation for this discrepancy is the position of the points on the 9-Dot specimen. While the view of the OOIs is limited in the uniaxial direction, both upwards and downwards, and the longitudinal strain is significantly underestimated, also due to the barrelling effect, the lateral deformation can be more accurately identified by the camera system. Consequently, the DIC results of the 9-Dot method for lateral strain appear to be representative of the actual deformation even at higher strain. The advantage over manual recording lies in the automated evaluation, which is particularly beneficial when working with multiple specimens.

In light of the aforementioned findings, the simulations were conducted using the lateral strain determined through the utilisation of 9-Dot DIC as the input parameter, in accordance with the methodology

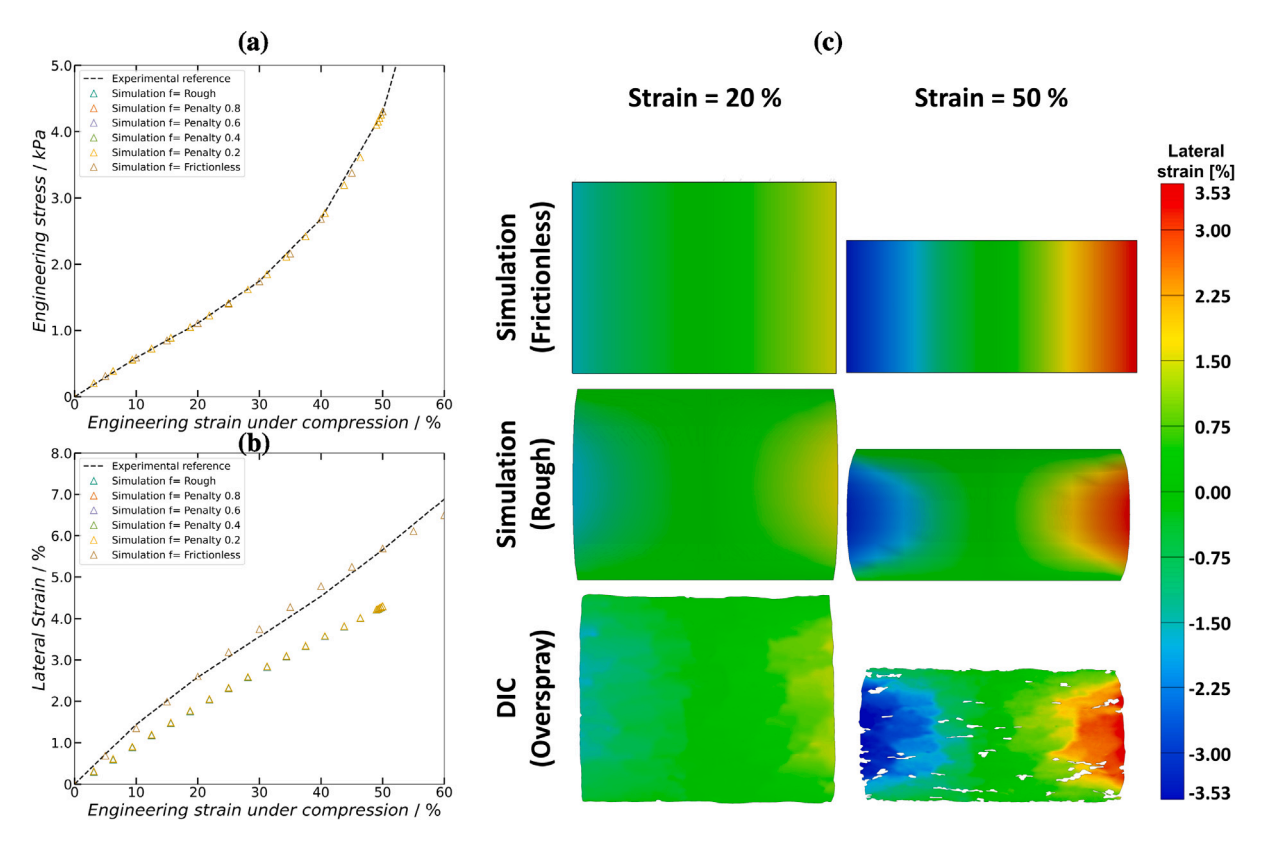


Fig. 7. Results of finite element analysis (FEA) (a) Comparison of the experimental stress–strain curve with the simulation results as a function of friction between aerogel and pressure plates (b) Comparison of the DIC overspray lateral strain with the simulation results as a function of friction between aerogel and pressure plates and compressive strain (c) Comparison of deformation in terms of the lateral strain surface distribution of simulation and DIC overspray at 20% and 50% compressive strain. The barrelling effect can be captured by introducing frictional contacts during the FE modelling.

Table 5
Sum of the squared error of the simulation data to the experimental reference as a function of friction and mesh size.

| | Values \ kPa² | | | | | |
|-----------------------------|-----------------------|------------------------|-----------------------|------------------------|------------------------|----------------------|
| | f = Rough | f = Penalty 0.8 | f = Penalty 0.6 | f = Penalty 0.4 | f = Penalty 0.2 | f = Frictionless |
| MSE Fine mesh (M = 1) | 10.94 ₁₀₋₅ | 10.99 ₁₀ -5 | 10.96 ₁₀₋₅ | 10.02 ₁₀ -5 | 10.87 ₁₀ -5 | 5.86 ₁₀₋₅ |
| MSE Standard mesh $(M = 2)$ | 13.4810-5 | 13.45 ₁₀₋₅ | 13.45 ₁₀₋₅ | 13.40 ₁₀₋₅ | 13.30 ₁₀₋₅ | 5.86 ₁₀₋₅ |
| MSE Coarse mesh $(M = 3)$ | 16.99 ₁₀₋₅ | 16.91 ₁₀₋₅ | 16.89 ₁₀₋₅ | 16.82 ₁₀₋₅ | 16.66 ₁₀₋₅ | 5.86 ₁₀₋₅ |

previously outlined. Firstly, the longitudinal stress–strain results of the simulations are presented in Fig. 7a. The representative experimental stress–strain curve is illustrated with a dashed line. The simulation results for varying friction values are also illustrated with triangular symbols. It is evident that there is an exact correlation between the friction-related simulation results and the experimental reference. Furthermore, it is noteworthy that even at higher magnification, no significant impact of friction on the stress–strain curve is noticeable. The greatest difference among the simulated results is given for the frictionless contact, which can most likely be attributed to the omission of the corresponding term during calculation. A more detailed look of this can be obtained by deriving the sum of the squared difference between the simulated results and the reverence curve, as illustrated in Table 5.

Overall, a satisfactory fit of the observed deviations from the reference for the various friction values can be observed. Additionally, the data indicates that the results for lower friction values show a marginally superior fit. Since the actual friction between the flexible silica aerogel and the pressure plates is unknown, this could be indicative of this value being effectively disappearing. Additionally, the variation in mesh size also demonstrates that the results are not significantly dependent on the three mesh sizes studied, indicating a stable simulation.

Nevertheless, the simulation presented here was only able to achieve convergence up to a compressive strain of 50%–60%. Furthermore, the simulation is unable to process experimental data with the desired level of accuracy. The experimental data (e.g., the lateral strain determined by DIC) may not be adequately represented by the hyperfoam model employed, as significant deformations occurring at higher compressive strains cannot be accurately reflected in this manner. One indication of this could be that full convergence up to 80% compression only occurs with frictionless contact, which in turn does not reflect the barrelling effect observed in the experiment. However, a barrelling effect as well as the interaction between material and pressure plate can already be observed at compressive strains of approx. 40%–50%. Consequently, an influence of friction on the stress and its distribution, if present, should be observable.

In addition to the stress–strain results, the effects of friction on the deformation of the specimen are also relevant, particularly if the model is to be used as a digital twin. To this end, the experimental lateral strain, determined using the DIC 9-Dot method and serving as input, is compared with the simulation results in Fig. 7b and displayed as a function of the compression and friction values. In the simulations, the lateral strain was calculated as the mean lateral increase in length across the entire model height.

It is notable that the simulation results exhibit a greater discrepancy from the reference than the ones from the stress–strain curves. As these differences increase with greater deformation, an explanation for this phenomenon could be that the simulation is only able to imitate the strong barrelling observed at greater deformation to a limited extent. Once more, the most accurate results were obtained with frictionless contact. It should be noted, however, that no barrelling is taken into account here, which means that the actual deformation cannot be imitated

In order to facilitate a more accurate assessment of the fidelity of the simulation in reproducing the actual deformation, the lateral strain distribution obtained from the simulation is directly compared with the lateral strain data obtained from the overspray DIC method, as illustrated in Fig. 7c. As previously established, the DIC results of the overspray method are only reproducible up to moderate deformations. Therefore, only compressive strains up to a maximum of 50% are used in this instance. The respective detected and simulated lateral strain is compared across the outer specimen surface, that is to say, from a lateral perspective. The scale displayed is identical for all colour-gradings shown.

The bottom row displays the experimental lateral strain recorded with overspray DIC. The observed distribution aligns with the anticipated outcomes, wherein the highest lateral strain is concentrated in the outer central region of the specimen, attributable to the barrelling effect and the constraints imposed by the pressure plates at the upper and lower parts of the specimen. This distribution becomes even more pronounced from 20 to 50% compressive strain, whereby the discontinuous colour transition is likely attributable to QOI errors and local differences in the concentration of the sprayed speckles, which can result in disparate mean values in areas of higher QOI density. A comparison of the simulation results with the actual deformation reveals that the lateral strain over the entire surface of the friction model is in excellent agreement. In the absence of barrelling, the deformation behaviour of the frictionless simulation, on the other hand, cannot be accurately represented.

In conclusion, it can be stated that the use of the DIC 9-Dot input has enabled the creation of a simulation of the flexible silica aerogel that is capable of mimicking the stress–strain behaviour and deformation of the specimen with a high degree of accuracy. The simulation is limited to approximately 50%–60% compression, as convergence issues arise when the deformation is more excessive. These could be optimised in the future by adapting the model used or the test input. With regard to model accuracy, it can also be demonstrated that the influence of friction on the stress–strain behaviour is negligible (order of magnitude approx. 10^{-2} to 10^{-3}). However, it is of great importance for the deformation behaviour of the specimen, especially in the case of strong compression.

4. Conclusions

This work presents the successful synthesis of flexible silica aerogels with reproducible geometry, using moulding devices, and an analysis of their mechanical properties using tensile and compression tests. Cyclic loading within the compression tests enables, among other things, the determination of a strain-dependent elastic modulus and allows the flexibility of the silica aerogel to be investigated. Tests demonstrated that even under very high compressive deformation up to 80%, the material exhibited a residual strain of only 4%–5%.

Furthermore, the elongation (longitudinal and lateral) of the material was recorded using digital image correlation (DIC) by utilising a reproducible 2D setup consisting of two different cameras. The results obtained using the classic overspray pattern method and a simplified 9-Dot pattern method for tensile tests were found to be in good agreement with the traverse path. A sensitivity analysis was conducted to identify suitable correlation parameters that demonstrated satisfactory accuracy for both models under compressive loading up to moderate compressive strains of approximately 50%. It was demonstrated that the overspray method has the benefit of accurately capturing the strain distribution,

whereas the simplified 9-Dot method yielded more precise results for the stress-strain curves under compression. It is recommended that further tests be conducted in the future using the 9-Dot method and varying the QOI positions. The number of QOIs should be sufficient to compensate for drift effects from other QOIs, but not so large as to render the QOI creation process unfeasibly time-consuming.

Finally, a material model was constructed using the Hyperfoam model within the FEA software Abaqus. This was done on the basis of the experimental results and the lateral strain curve of the DIC 9-Dot method. It was demonstrated that the impact of friction between the flexible silica aerogel and the pressure plates on the stress–strain behaviour under compression is negligible, which can be attributed to the flexibility of the material. However, it must be accounted for in the model to capture the barrelling effect.

The analysis and sensitive DIC study set up in this work facilitate a comprehensive and reproducible analysis of flexible materials. It can therefore be concluded that the experimental data presented here can be used as a basis for material models, on which further investigations can be carried out, provided that sufficient experimental data is collected. In conclusion, these methods offer a previously unavailable insight into the mechanical properties and influencing factors of flexible aerogels, which can facilitate the advancement of material development and verification for practical applications.

CRediT authorship contribution statement

Max Zinke: Writing – original draft, Visualization, Validation, Methodology, Investigation, Formal analysis. Barbara Milow: Writing – review & editing, Funding acquisition. Gunnar Seide: Writing – review & editing, Supervision. Ameya Rege: Writing – review & editing, Supervision, Methodology, Funding acquisition, Conceptualization.

Declaration of competing interest

The authors declare that they have no known competing financial interests or personal relationships that could have appeared to influence the work reported in this paper.

Appendix A. Supplementary data

Supplementary material related to this article can be found online at https://doi.org/10.1016/j.mechmat.2025.105510.

Data availability

Data will be made available on request.

References

Almeida, C.M., Ghica, M.E., Ramalho, A.L., Durães, L., 2021. Silica-based aerogel composites reinforced with different aramid fibres for thermal insulation in space environments. J. Mater. Sci. 56 (24), 13604–13619.

Bhuiya, M.M.H., Anderson, A.M., Carroll, M.K., Bruno, B.A., Ventrella, J.L., Silberman, B., Keramati, B., 2016. Preparation of monolithic silica aerogel for fenestration applications: Scaling up, reducing cycle time, and improving performance. Ind. Eng. Chem. Res. 55 (25), 6971–6981.

Fekadu, B., Rege, A., Heyer, M., Besel, Y., Milow, B., Bartsch, M., 2022. Mechanisches Verhalten von Silica-Aerogelen in Abhängigkeit von der Druckdehnung. Tagungsband "Werkstoffprüfung 2022".

Fener, R., Niemeyer, P., 2016. Flexible Komposite auf Basis von Aerogelen. Patent EP 3 042 884 B1.

Guo, H., Nguyen, B.N., McCorkle, L.S., Shonkwiler, B., Meador, M.A.B., 2009. Elastic low density aerogels derived from bis [3-(triethoxysilyl) propyl] disulfide, tetramethylorthosilicate and vinyltrimethoxysilane via a two-step process. J. Mater. Chem. 19 (47), 9054–9062.

Haj-Ali, R., Eliasi, R., Fourman, V., Tzur, C., Bar, G., Grossman, E., Verker, R., Gvishi, R., Gouzman, I., Eliaz, N., 2016. Mechanical characterization of aerogel materials with digital image correlation. Microporous Mesoporous Mater. 226, 44–52.

- Hayase, G., Kanamori, K., Nakanishi, K., 2011. New flexible aerogels and xerogels derived from methyltrimethoxysilane/dimethyldimethoxysilane co-precursors. J. Mater. Chem. 21 (43), 17077–17079.
- Heyer, M., Berkefeld, A., Voepel, P., Milow, B., 2020. Advanced opacified fiber-reinforced silica-based aerogel composites for superinsulation of exhaust tubing systems in semi-stationary motors. Materials 13 (12), 2677.
- Hill, R., 1979. Aspects of invariance in solid mechanics. In: Yih, C.-S. (Ed.), In: Advances in Applied Mechanics, vol. 18, Elsevier, pp. 1–75.
- Hrubesh, L.W., 1998. Aerogel applications. J. Non-Cryst. Solids 225, 335–342.
- Hüsing, N., Schubert, U., 1998. Aerogels—airy materials: chemistry, structure, and properties. Angew. Chem. Int. Ed. 37 (1-2), 22-45.
- Jones, E., Iadicola, M., 2018. A good practices guide for digital image correlation.
- Marter, A.D., Dickinson, A.S., Pierron, F., Browne, M., 2018. A practical procedure for measuring the stiffness of foam like materials. Exp. Tech. 42 (4), 439–452.
- Merillas, B., Lamy-Mendes, A., Villafañe, F., Durães, L., Rodríguez-Pérez, M.Á., 2022a. Silica-based aerogel composites reinforced with reticulated polyurethane foams: Thermal and mechanical properties. Gels 8 (7), 392.
- Merillas, B., Lamy-Mendes, A., Villafañe, F., Durães, L., Rodríguez-Pérez, M., 2022b. Polyurethane foam scaffold for silica aerogels: effect of cell size on the mechanical properties and thermal insulation. Mater. Today Chem. 26, 101257.
- Merzkirch, M., 2022. Mechanical Characterization Using Digital Image Correlation.
- Ogden, R.W., Hill, R., 1972. Large deformation isotropic elasticity on the correlation of theory and experiment for incompressible rubberlike solids. Proc. R. Soc. A 326 (1567), 565–584.

- Parmenter, K.E., Milstein, F., 1998. Mechanical properties of silica aerogels. J. Non-Cryst. Solids 223 (3), 179–189.
- Patil, S.P., Rege, A., Sagardas, Itskov, M., Markert, B., 2017. Mechanics of nanostructured porous silica aerogel resulting from molecular dynamics simulations. J. Phys. Chem. B 121 (22), 5660–5668.
- Rao, A.V., Bhagat, S.D., Hirashima, H., Pajonk, G., 2006. Synthesis of flexible silica aerogels using methyltrimethoxysilane (MTMS) precursor. J. Colloid Interface Sci. 300 (1), 279–285.
- Rege, A., Schwan, M., Chernova, L., Hillgärtner, M., Itskov, M., Milow, B., 2020. Microstructural and mechanical characterization of carbon aerogels: An in-situ and digital image correlation-based study. J. Non-Cryst. Solids 529, 119568.
- Rege, A., Voepel, P., Okumus, E., Hillgärtner, M., Itskov, M., Milow, B., 2019. Temperature-dependent stiffening and inelastic behavior of newly synthesized fiber-reinforced super flexible silica aerogels. Materials 12 (18), 2878.
- Schwan, M., Rößler, M., Milow, B., Ratke, L., 2015. From fragile to resilient insulation: synthesis and characterization of aramid-honeycomb reinforced silica aerogel composite materials. Gels 2 (1), 1.
- Smirnova, I., Gurikov, P., 2018. Aerogel production: Current status, research directions, and future opportunities. J. Supercrit. Fluids 134, 228–233.
- Storåkers, B., 1986. On material representation and constitutive branching in finite compressible elasticity. J. Mech. Phys. Solids 34 (2), 125–145.
- Zu, G., Shimizu, T., Kanamori, K., Zhu, Y., Maeno, A., Kaji, H., Shen, J., Nakanishi, K., 2018. Transparent, superflexible doubly cross-linked polyvinylpolymethylsiloxane aerogel superinsulators via ambient pressure drying. Acs Nano 12 (1), 521–532.